On the Micromechanics of Voids in Nanotwinned Materials

Kartikey Joshi[1,2] and Shailendra P. Joshi[3*]

[1] Department of Mechanical Engineering, National University of Singapore, Singapore 117576
[2] Institute of High Performance Computing, Singapore 138632
[3] Department of Mechanical Engineering, University of Houston, Houston, TX 77204-4006, USA

May 6, 2022

Abstract

This work investigates internal damage by void growth in NT microstructures via crystal plasticity. The framework incorporates length-scale effects and explicitly models twin boundary migration. Using finite-deformation, plane strain finite element calculations of porous unit cells, we analyze the roles of twin size, plastic anisotropy and twin boundary migration on void evolution over a range of controlled biaxial stress states. The simulations provide insights into crystallographic aspects of porosity growth in NT microstructures. Emphasis is placed on correlating the micromechanics of failure by internal necking. Irrespective of the level of crystallographic plastic anisotropy, twin boundary migration effectively shields the void growth process, delaying the porosity evolution compared to non-twinned microstructures. It is found that crystallographic plastic anisotropy causes kink band instability that can affect void growth. Coupled with twin boundary mobility, twin size and crystallographic plastic anisotropy create a rich landscape of failure characteristics as a function of the stress state.

*Corresponding author: shailendra@uh.edu

1 Introduction

Damage tolerance is described via macroscopic quantities such as tensile ductility, deformation stability, and toughness, which emerge as a result of generation and evolution of voids and cracks, or shear bands at the microstructural scales [51]. In metals, simultaneous improvement of strength and damage tolerance is a thorny challenge. Strategies to improve damage tolerance rely on microstructural engineering to enhance strain hardening and strain rate sensitivity, which are known to stabilize plastic deformation; see Pineau et al. [52] for an excellent overview on this topic.

Since the seminal work of Lu et al. [41], nanotwinned (NT) metals have piqued the interest in designing strong, damage-tolerant microstructures with engineered interfaces [10, 19, 39, 42, 69, 73, 82]. In addition to offering a way to addressing the strength-ductility trade-off [40, 87], NT materials exhibit good electrical conductivity [29, 41] and radiation damage tolerance [4].

While twin boundaries serve as agents of strengthening via novel plasticity mechanisms, they also cause yield softening via twin boundary (TB) migration [36, 40, 58, 72]. These mechanisms can have a profound effect on the mechanisms of damage and ultimate fracture [35]. Fracture surfaces of NT copper (NT Cu) show ductile failure forensics with dimples that are much larger than the average twin and grain sizes [55]. Experiments and atomistic simulations indicate crack arrest at twin boundaries thereby providing toughening mechanisms [32, 81] and resulting in improved fracture toughness [84] via TB migration. Atomistic simulations reveal that NT nanowires with an initial pre-crack along a TB may exhibit brittle-to-ductile transition below a critical twin size [25], and intrinsic asymmetry in fracture responses (ductile versus brittle) of twin boundaries [9, 61].

A few criteria have been proposed to quantify twin size dependent macroscopic ductility of NT materials. Dao et al. [13] propose a fracture criterion based on theoretical maximum local plastic displacement due to twin partial slip, which serves as a soft deformation mode. A different local criterion for ductility proposed by Zhu et al. [86] is based on the condition that the local flow stress in the twin lamellas and grain boundaries equals the critical stress required for the homogeneous nucleation of dislocations. It predicts that for large twin sizes ($\gtrsim$ 10 nm), failure preferentially occurs within the twin lamellas, with ductility increasing gradually as the twin spacing is reduced. For hierarchical NT architectures, the criterion predicts that the failure strain increases with decreasing spacing of the primary twins (for fixed secondary twin spacing); for fixed primary twin spacing, failure strain is shown to decrease with decreasing secondary twin spacing [85]. While these efforts provide useful insight, they conceal the underlying micromechanics of damage evolution in NT microstructures. Crystal plasticity simulations by Jerusalem et al. [26] suggest that such propositions may be insufficient and that it is important to understand the role of void evolution in the damage behaviors of NT microstructures [76]. Indeed, in NT materials nanovoids may nucleate ahead of crack tips and at twin boundary-grain boundary triple junctions during deformation [48, 80, 84], or may preexist due to vacancy clustering [12, 68]. *In situ* transmission electron microscopy tensile experiments reveal formation and growth of nanovoids in silver NT wires, but a lack thereof in nanowires without twins [83].

Insofar as the micromechanics of void growth in NT materials is concerned, several questions arise: *How does the presence and migration of TBs affect void evolution? What is the role of twin size in this interaction? How do these micromechanical features govern material ductility under multiaxial stress states?*

In conventional materials, grain-scale plastic anisotropy is attributed to crystal lattice orientation with respect to loading axes. In NT materials, the grain-scale plastic anisotropy has an additional contribution, which arises from the difference in the grain size and twin size. In essence, the crystallographic strengths of slip systems parallel to a twin boundary may be different from those inclined to the twin boundary. This latter aspect appears to play a role in the damage toler-

ance of NT materials [78, 87]. Singh et al. [60] reveal that decreasing twin size (at a fixed grain size) improves ductility, fracture toughness, and fatigue characteristics in electrodeposited NT Cu. More recent experiments [79] show approximately two-fold increase in the tensile ductility and fracture toughness of the electrodeposited NT Cu with a four-fold increase in grain size while keeping the twin thickness nearly the same.

Early modeling efforts of porous single crystals indicate that crytallographic plastic anisotropy has an effect on the void growth. For porous face-centered-cubic (FCC) single crystals undergoing asymmetric slip, void growth occurs under nominally uniaxial plane strain loading unlike their counterparts undergoing symmetric slip [45]. Subsequent crystal plasticity studies reveal a strong effect of crystallographic orientation on void shapes and void growth rates [37, 53, 62, 63, 66, 77]. For instance, porosity evolution is reported to be the fastest for [111] crystal orientation [54] and can occur even under uniaxial stress conditions [66]. While these and associated studies do not account for length-scale effects, seminal developments in gradient plasticity have revealed delayed void growth due to strain gradient effects [16, 17, 23]. Since then, significant progress has been achieved in understanding length-scale effects in void growth through continuum [e.g., 18, 31, 64, 65, 75] and gradient crystal plasticity [e.g., 7, 24, 59] approaches. That said, these and similar investigations essentially limit the scope of microstructural aspects to crystal orientations.

In this paper, we adopt a length-scale dependent discrete twin crystal plasticity approach to simulate twin-void interactions under multiaxial loading states. The emphasis is on understanding the roles of TB migration, size effects, and plastic anisotropy on the micromechanics of void growth and coalescence under controlled tensile stress states.

2 Discrete Twin Crystal Plasticity

The length-scale dependent crystal plasticity model adopted here [28] postulates a small but finite *twin boundary affected zone* (TBAZ) in the vicinity of each TB embedded in a single crystal. The remaining part of the twin lamella is notionally referred to as the *bulk* region. In both regions, the slip systems are categorized into two families: a family of 3 slip systems that are coplanar to the TB and a family of 9 slip systems that are non-coplanar. The coplanar slip systems in the TBAZ models the twin partial slip that results in TB migration. We describe the basic features of the model.

The total deformation gradient is decomposed as $\mathbf{F} = \mathbf{F}^e\mathbf{F}^p$ where $\mathbf{F}^e$ and $\mathbf{F}^p$ are the elastic and plastic parts, respectively. The resulting velocity gradient is:

$$\mathbf{L} = \mathbf{L}^e + \underbrace{\mathbf{F}^e\tilde{\mathbf{L}}^p\,(\mathbf{F}^e)^{-1}}_{\mathbf{L}^p} \tag{1}$$

where $\mathbf{L}^e$ and $\mathbf{L}^p$ are the elastic and plastic parts in the current configuration. Assuming that Schmid law applies, the plastic velocity gradient ($\mathbf{L}^p$) has contributions from the slip rates ($\dot{\gamma}$) on the slip and twinning dislocation systems

$$(\mathbf{L}^p)_{\text{bulk}} = \underbrace{\sum_{\alpha=1}^{3}\dot{\gamma}^{\alpha}(\boldsymbol{s}^{\alpha}\otimes\boldsymbol{m}^{\alpha})}_{\text{coplanar slip}} + \underbrace{\sum_{\beta=4}^{12}\dot{\gamma}^{\beta}(\boldsymbol{s}^{\beta}\otimes\boldsymbol{m}^{\beta})}_{\text{non-coplanar slip}} \tag{2}$$

$$(\mathbf{L}^p)_{\text{TBAZ}} = \underbrace{\sum_{\alpha'=1}^{3}\dot{\gamma}_{\text{tp}}^{\alpha'}(\boldsymbol{s}^{\alpha'}\otimes\boldsymbol{m}^{\alpha'})}_{\text{coplanar slip}} + \underbrace{\sum_{\beta=4}^{12}\dot{\gamma}^{\beta}(\boldsymbol{s}^{\beta}\otimes\boldsymbol{m}^{\beta})}_{\text{non-coplanar slip}} \tag{3}$$

where $\boldsymbol{s}^i$ and $\boldsymbol{m}^i$ ($i = \alpha, \beta, \alpha'$) are slip directions and slip plane normals in the current configuration, respectively. Eq. (2) refers to the slip systems in the bulk region while Eq. (3) refers to the slip contribution in the TBAZ. For convenience, using (111) as the reference twin plane we split the slip system descriptions in each of these regions into two contributions: co-planar and non-coplanar. While the coplanar and non-coplanar slip in the bulk region is assumed to be via glide of *full* dislocations (i.e. $\{111\}\langle 110\rangle$), coplanar slip (on the (111) plane) in TBAZ is assumed due to twinning partials only, i.e. $(111)\langle 11\bar{2}\rangle$. It is this twin partial slip activity that enables twin boundary migration. Non-coplanar slip in TBAZ is assumed to evolve via slip on the remaining $\{111\}\langle 110\rangle$.

The co-rotational increment of the Cauchy stress tensor ($\Delta\sigma_{ij}$) is calculated as

$$\Delta\sigma_{ij} = L_{ijkl}\Delta\varepsilon_{kl} - \sigma_{ij}\Delta\varepsilon_{kk} - \sum_{\alpha}\left[L_{ijkl}\mu^{\alpha}_{kl} + \omega^{\alpha}_{ik}\sigma_{jk} + \omega^{\alpha}_{jk}\sigma_{ik}\right]\Delta\gamma^{\alpha} \tag{4}$$

where $\Delta\boldsymbol{\varepsilon}$ is the incremental total strain tensor and $\Delta\gamma^{\alpha}$ is the incremental plastic slip on slip system α; $\boldsymbol{\mu}^{\alpha}$ and $\boldsymbol{\omega}^{\alpha}$ are:

$$\mu^{\alpha}_{ij} = \frac{1}{2}\left[s^{\alpha}_i m^{\alpha}_j + s^{\alpha}_j m^{\alpha}_i\right]; \quad \omega^{\alpha}_{ij} = \frac{1}{2}\left[s^{\alpha}_i m^{\alpha}_j - s^{\alpha}_j m^{\alpha}_i\right] \tag{5}$$

The elastic stiffness tensor $\mathbb{L}$ is obtained by rotating the local stiffness tensor $\mathbb{L}^*$ defined in the crystal coordinate system to the global (laboratory) coordinate system with a crystallographic rotation matrix $\mathbf{R}$ as $L_{ijkl} = R_{ijpq}L^*_{pqrs}R_{rskl}$.

2.1 Bulk plasticity

To account for TB strengthening, we consider that the viscoplastic slip-rate $\dot{\gamma}^i$ (Eq. (2)) on a slip system i is:

$$\dot{\gamma}^i = \dot{\gamma}_0\left|\frac{\tau^i}{\hat{g}^i}\right|^{1/m_{\mathrm{b}}}\mathrm{sign}(\tau^i) \tag{6}$$

where τ^i is the resolved shear stress on the slip system, m_{b} the rate sensitivity parameter of the bulk, and $\hat{g}^i$ the current size-dependent slip resistance given by,

$$\hat{g}^i = \tau^i_0\sqrt{\left(\frac{g^i}{\tau^i_0}\right)^2 + l_g\eta^i_g} \tag{7}$$

where τ^i_0 is the size-dependent initial CRSS and g^i is the current strength of slip system i from the size-independent hardening [50]:

$$g^i = \tau^i_0 + \int_0^t \dot{g}^i \,\mathrm{d}t; \quad \dot{g}^i = H(\bar{\gamma})\dot{\gamma}^i; \quad H(\bar{\gamma}) = h_0\,\mathrm{sech}^2\left|\frac{h_0\bar{\gamma}}{h_{\mathrm{s}}}\right| \tag{8}$$

where h_0 and h_{s} are material hardening parameters.

The size-dependent hardening in Eq. (7) is modeled via the effective density of the geometrically necessary dislocations [21]:

$$\eta^i_g = \left|\boldsymbol{m}^i \times \sum_j [\boldsymbol{s}^i \cdot \boldsymbol{s}^j]\boldsymbol{\nabla}\gamma^j \times \boldsymbol{m}^j\right| \tag{9}$$

where $\boldsymbol{\nabla}\gamma^j$ represents the spatial gradient of γ^j [21]; the computational details of calculating the gradients are in the Appendix. The material length-scale, l_g, is associated with the average spacing between obstacles to dislocation motion [15].

In the original model [28], we modeled the yield strengthening effect by incorporating slip-rate gradients [20] in the calculation of τ_0^i (Eq. (7)). However, such a calculation becomes prohibitive for the current investigation. Therefore, we adopt a simplified approach to model this effect. Motivated by the results in Joshi and Joshi [28], these size effects are approximated via Hall-Petch type relations at the crystallographic scale:

$$\tau_0^\alpha = g_0 \left(\frac{d_c}{d_0}\right)^{0.5} \qquad (\alpha = 1-3) \quad ; \quad \tau_0^\beta = g_0 \left(\frac{\lambda_c}{\lambda_0}\right)^{0.5} \qquad (\beta = 4-12) \tag{10}$$

where g_0 is the size-independent initial CRSS of a single crystal, λ_0 and d_0 are the initial twin size and grain size respectively, and λ_c and d_c the critical grain and twin sizes such that $\tau_0^\alpha = g_0$ if $d_0 > d_c$ and $\tau_0^\beta = g_0$ if $\lambda_0 > \lambda_c$. Grain boundaries (i.e., d_0) are not explicitly modeled, although we do consider a scenario where $\tau_0^\alpha = \tau_0^\beta$, which implies $d_0 = \lambda_0$.

2.2 Interfacial plasticity and twin boundary migration

The TBAZ region accrues plasticity via coplanar and non-coplanar slip processes, cf. Eq. (3). The non-coplanar slip on a slip system β is given by:

$$\dot{\gamma}^\beta = \dot{\gamma}_0 \left|\frac{\tau^\beta}{g_z}\right|^{1/m_b} \text{sign}(\tau^i)$$

where $g_z = U^* l_{act}/\Omega$ is governed by the energy barrier U^* for dislocation-TB interactions with $\Omega = \xi b^3$ as the activation volume that linearly varies with λ_0 [2, 71] and l_{act} the distance over which a reaction occurs.

The coplanar slip in the TBAZ effectively models TB migration as follows. Broadly, two processes affect TB migration: (i) source-driven: twinning partial nucleation from triple junctions a lá [36], and (ii) reaction driven: TB interfacial dislocations arising from myriad TB-lattice dislocation interactions [88, 89]. In Joshi and Joshi [28], we proposed a model based on twin partial plasticity, which is briefly described here.

The slip-rate on coplanar slip systems in the TBAZ are assumed to follow the following rule:

$$\dot{\gamma}_{\text{tp}}^{\alpha'} = \underbrace{\dot{\gamma}_0 \left(\frac{\tau_{\text{tp}}^{\alpha'}}{\tau_0^{\text{tp}}}\right)^{1/m_t} \text{sign}(\tau_{\text{tp}})}_{\text{source driven}} + \mathcal{Y} \left[\underbrace{\dot{\gamma}_0 \left(\frac{\tau_{\text{tp}}^{\alpha'}}{\tau_{\text{fric}}}\right)^{1/m_t} \text{sign}(\tau_{\text{tp}})}_{\text{interfacial reaction driven}}\right] ; \quad \mathcal{Y} = \begin{cases} 0, & \text{if } (\tau_{\max}^\beta/g_z) < 1 \\ 1, & \text{if } (\tau_{\max}^\beta/g_z) \geq 1 \end{cases} \tag{11}$$

where m_t is the TBAZ strain rate sensitivity parameter and $\tau_{\text{tp}}^{\alpha'}$ is the resolved shear stress on the twin partial slip system α'.

In Eq. (11), $\tau_0^{\text{tp}} = \dfrac{U_0}{\Omega_n} + \dfrac{kT}{\Omega_n} \ln\left[\dfrac{1}{\gamma_{\text{tw}}} \dfrac{\dot{\gamma}_0}{\nu_0} \left(\dfrac{N^*}{N^s}\right)\right]$ is the CRSS required for the nucleation of twinning partials from triple junctions (e.g., twin boundary-grain boundary, twin boundary-free surface, with U_0 as the activation energy, Ω_n the activation volume, ν_0 the attempt frequency, (N_s/N^*) the ratio of the number of twin partial sources to the number of atomic planes in the TBAZ, respectively, k the Boltzmann constant [44]).

The second term on the right side of Eq. (11) is explained as follows: the prerequisite for TB migration driven by non-coplanar dislocations is that the interfacial reactions have indeed occurred. This may be viewed as *yielding* of the TBAZ, which is tracked through the parameter $\mathcal{Y}$ in Eq. $(11)_2$ where $\tau^{\beta}_{\max}$ is the RSS on the most active non-coplanar slip system in the TBAZ. Once the condition $\mathcal{Y}$ is satisfied, twin partial activity on the TB is driven by the lattice friction stress τ_{fric}.

Defining $\gamma_{\text{tp}}(t) \equiv \int_0^t \dot{\gamma}_{\text{tp}} \mathrm{d}t'$ as the accumulated twin partial shear strain, twinning induced lattice reorientation of the TBAZ occurs when $\gamma_{\text{tp}} = \gamma_{\text{tw}}$ where γ_{tw} is the twinning shear strain. Effectively, the twin boundary migrates by the distance equal to the TBAZ thickness. The details of this process are presented in Mirkhani and Joshi [44].

The foregoing model is implemented in ABAQUS/ STANDARD® as a user-material (UMAT) subroutine that is based on Huang [22].

Before discussing the results, we note three aspects. First, we only model the evolution of twinned structure by TB migration and do not model nucleation of new nanotwins. Second, we ignore the role of surface energy in void evolution, which could become important if the void size ($d_0 \lesssim \gamma_{\text{s}}/\tau_0$) where γ_{s} is the surface energy and τ_0 is an appropriate CRSS [18]. The third aspect pertains to the mechanism of twin boundary migration. On a given (111) twin plane, three partial Burgers vectors can glide, $\boldsymbol{b}_1 = [11\bar{2}], \boldsymbol{b}_2 = [2\bar{1}\bar{1}], \boldsymbol{b}_3 = [\bar{1}2\bar{1}]$. We assume that each twin partial nucleated on the (111) twin plane has the same Burgers vector, say $\boldsymbol{b}_1$. Referring to Eq. (11), this implies that $\dot{\gamma}^{\alpha'}_{\text{tp}} = 0$ for $\alpha' = 2, 3$. Such a process is referred to as *monotonic activation of partials* (MAP, [74]). By way of consequence, each TB migration event by one atomic plane generates a twinning shear strain (γ_{tw}) in the same direction so that at time t there is a macroscopic maximum shear deformation corresponding to the total shear strain generated by the glide of twin partials with identical Burgers vector. The other extreme is *cooperative activation of partials* (CAP) where N successive TB migration events comprise equal number of the activation events of the three Burgers vectors, which results in a net zero macroscopic shear deformation (given that $\boldsymbol{b}_1 + \boldsymbol{b}_2 + \boldsymbol{b}_3 = 0$). A more general scenario of TB migration is via *random activation of partials* (RAP) where the choice of twin partial Burgers vector on successive planes is random and as a result, the accrued shear deformation depends on the net sum of the three Burgers vectors. In all three scenarios, the magnitude of the shear strain accrued is the same for the amount by which the twin boundary migrated. In principle, it is possible to consider either CAP or RAP within the current framework but it requires additional book-keeping, and is not the focus of this work.

3 Computational Setup

Fig. 1 shows fully periodic, 2D porous unit cells considered in this work. Along with the reference case of a single crystal, we consider several NT microstructures with initial twin lamella sizes $\lambda_0 \in \{25\text{nm}, 50\text{nm}, 100\text{nm}\}$, succinctly referred to as NT25, NT50 and NT100, respectively (Fig. 1a-1d). We adopt the approach by Tekoglu et al. [67] to maintain a constant state of biaxial stress (see Joshi [27] for details). Each microstructure is discretized using a refined mesh of more than ~ 3000 plane strain finite elements (CPE4). The choice of this mesh density is based on a prior mesh sensitivity study for pristine unit cells in the presence of slip-gradients ensuring at least 10 finite elements along the thickness of a twin lamella, see Joshi [27] for details. The initial porosity $f_0 = V_{\text{void}}/V_{\text{cell}}$ where V_{void} and V_{cell} are the initial volumes of the void and unit cell. The TBAZ thickness is assumed to be 2 nm [28]. The unit cell has an initial width $W_0 = 52$ nm and a height $H_0 = 200$ nm, which sets the spacing between voids given the periodic boundary conditions. We consider a cylindrical void with an initial diameter of 10 nm, which gives $f_0 = 0.7\%$. The initial twin volume fraction is $\xi_0 = V_{\text{twin}}/V_{\text{cell}}$ where V_{twin} is the initial volume of the twinned region. We consider

equi-sized twins (Fig. 1b-1d), i.e. $\xi_0 = 0.5$, so that both the *matrix* and *twinned* regions have the same volume initially. The choice of this unit cell is motivated by several considerations. Along the x_2-axis, H_0 keeping the mesh consistent across the different microstructures while ensuring that the TB migration mechanics for the largest twin lamella (100 nm) case can be modeled together with periodic boundary conditions. As for the x_1-dimension, the choice of W_0 gives an aspect ratio of 4, which is computationally much less expensive (than an aspect ratio of 1) by reducing the domain size and setting up an initial porosity, which keeps calculations tractable. A larger x_1 dimension would result in a very small initial porosity and the inter-void ligaments would be too large to obtain void coalescence within a tractable computational expense. Finally, the choice of horizontal twin boundaries is one of computational simplicity. Moreover, it eliminates the potential artifact of stepped twin boundaries that may occur for an inclined boundary discretized using a structured finite element grid.

The global x_1 and x_2 axes are respectively aligned with the crystallographic $[11\bar{2}]$ and $[111]$ directions and the void axis is along $[\bar{1}10]$, Fig. 1e. For brevity, we denote the non-coplanar slip systems on the plane $(11\bar{1})$ as β_1 and those on the $(1\bar{1}1)$ and $(\bar{1}11)$ as β_2. Thus, $\beta_1 \in \{(11\bar{1})[101], (11\bar{1})[011]\}$ and $\beta_2 \in \{(\bar{1}11)[101], [\bar{1}11)[110]\}$. In addition, the coplanar slip system pair is $\alpha \in \{(111)[\bar{1}01], (111)[0\bar{1}1]\}$. Experiments on NT microstructures indicate preferred orientations of this kind that arise from material synthesis [1, 8, 70]. Simulation studies of voided FCC single crystal unit cells [e.g., 6, 38, 66] reveal a rapid porosity evolution for this orientation relative to other orientations. As denoted in Fig. 1e, the α, β_1 and β_2 slip systems are modeled as full dislocations in the bulk region. Fig. 1f shows the arrangement of these pairs when observed in the x_1-x_2 plane. Within the TBAZ, while the non-coplanar slip is modeled as full dislocations, slip on the twin plane (ABC) is modeled via partial dislocations (α') represented by the segments δ-A, δ-B and δ-C. With reference to the MAP mechanism discussed in the preceding paragraph, we model the twin partial slip δ-C. In the computational setting, twin partial slip is initiated by mimicking the effect of a stress concentrator (e.g., a GB-TB triple junction, TB kink, or an intersection of an incoherent TB with a coherent TB) by prescribing a single finite element from each TBAZ as a nucleation source by reducing its elastic stiffness to 0.9 times the initial value. We ensure that this local stiffness reduction does not cause strain localization. Periodic boundary conditions set up the spacing between the nucleation sources. After each TB migration event, a new nucleation source is chosen at the updated TB location and the elastic stiffness of the old master element is reinstated to the original value. Once the resolved shear stress in the master element becomes equal to the CRSS for twin partial nucleation, (τ_0^{tp}), the TBAZ starts to accrue significant plasticity via twinning partial slip. TBAZ elements are reoriented from matrix to twinned configuration once the twinning condition ($\gamma^{\mathrm{tp}} = \gamma^{\mathrm{tw}}$) is satisfied.

Material properties (Table 1) resemble those of single crystal copper, with C_{11}=168.4 GPa, C_{12}=121.4 GPa and C_{44}=75.4 GPa. The magnitude of the material length-scale (l_g) is chosen to be in the range of the twin size and kept constant for simplicity. Likewise, the value for λ_c is chosen based on our previous work [28], which indicates that the crystallographic strengthening effect diminishes beyond a twin size $\sim 1 - 2\mu$m.

Table 1 Material parameters [cf. 28]

g_0 (MPa)	h_0 (MPa)	h_{s} (MPa)	τ_0^{tp} (MPa)	l_g (nm)	λ_c, d_c (nm)	$\dot{\gamma}_0$ (s^{-1})	m_{t}	m_{b}	U^* (eV/nm)	$l_{act} = b$ (nm)	Ω (nm^3)
60	540	50	20	50	1500	0.001	0.1	0.02	6.5	0.25	0.95-0.23

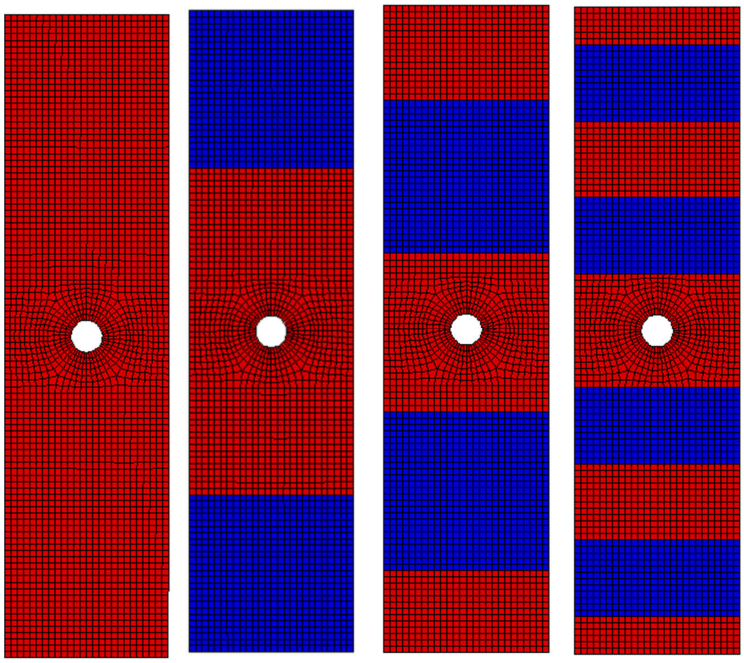

(a) single crystal **(b)** NT100 **(c)** NT50 **(d)** NT25

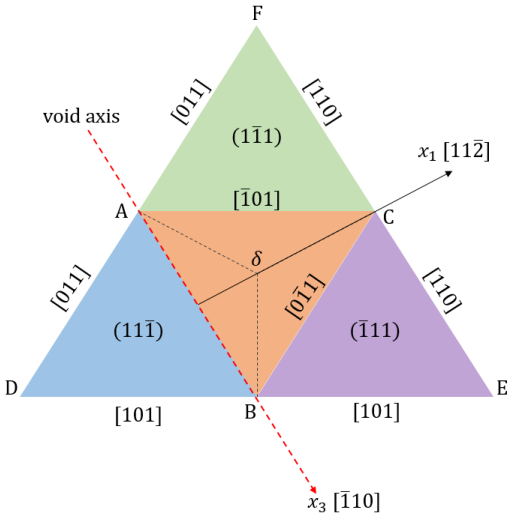

(e)

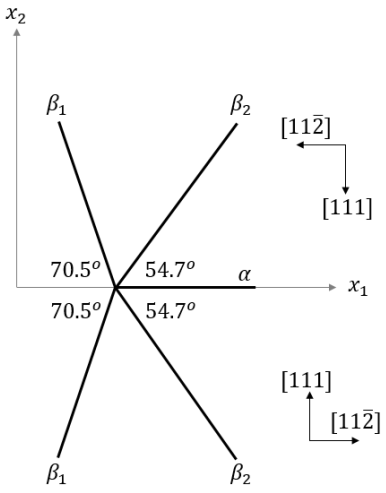

(f)

Figure 1 Panels (a-d) show microstructures with initial circular voids. In NT microstructures (panels b-d), blue and red regions represent twin variants. Panel (e) shows Thompson tetrahedron indicating the relative orientation of the void axis with respect of the crystal and global axes, and the slip systems. Panel (f) shows the α, β_1 and β_2 slip system pairs as seen in the $x_1 - x_2$ plane.

A nominal tensile strain rate $\dot{\varepsilon}_0 = 1 \times 10^{-3}$ s^{-1} is applied in the x_2 direction while maintaining a constant macroscopic biaxial stress state defined by the stress biaxiality ratio $\mathcal{B} = \Sigma_{11}/\Sigma_{22}$. We consider a range of biaxiality ratios, $\mathcal{B} \in \{0, 0.075, 0.2, 0.5\}$. The plane strain assumption implies $\Sigma_{33} \neq 0$; $\mathcal{B} = 0$ is tantamount to plane strain uniaxial loading.

The volume-averaged equivalent stress (Σ_{eq}) and equivalent strain (E_{eq}) are defined as:

$$\Sigma_{\text{eq}} = \frac{1}{\sqrt{2}}\sqrt{(\Sigma_{11}-\Sigma_{22})^2 + (\Sigma_{22}-\Sigma_{33})^2 + (\Sigma_{11}-\Sigma_{33})^2 + 6(\Sigma_{12}^2 + \Sigma_{23}^2 + \Sigma_{13}^2)} \tag{12}$$

$$E_{\text{eq}} = \frac{\sqrt{2}}{3}\sqrt{(E_{11}-E_{22})^2 + (E_{22}-E_{33})^2 + (E_{11}-E_{33})^2 + 6(E_{12}^2 + E_{23}^2 + E_{13}^2)} \tag{13}$$

where $\Sigma_{ij} = (1/V)\int \sigma_{ij} \mathrm{d}V$ is the volume-averaged stress component corresponding to the local stress component σ_{ij} and $E_{11} = \ln(W/W_0)$ and $E_{22} = \ln(H/H_0)$ are the nominal strains where W_0, H_0 are respectively the initial and unit cell width and height, and W, H are their current (at time t) values.

4 Results and Discussion

Polycrystal NT architectures may be instantiated using two microstructural length-scales: the average grain size (d_0) and the initial twin size (λ_0). These length-scales respectively modulate the coplanar and non-coplanar slip system strengths, cf. Eq. (10). The ratio $\kappa = \tau_0^{\beta}/\tau_0^{\alpha} = \sqrt{d_0/\lambda_0}$ serves as a measure of the slip strength anisotropy in the normal (non-coplanar) and shear (coplanar) directions with respect to the TB. For a fixed grain size along the x_1-direction, κ increases with decreasing initial twin size λ_0. Thus, for the NT100, NT50, and NT25 cases, $\kappa = 3.0, 4.5$, and 6.3 respectively. To understand the implications of anisotropy and the role of twin boundaries, we also consider additional cases: (a) isotropic twinned crystals ($\kappa = 1$), (b) isotropic single crystal ($\kappa = 1$), and (c) anisotropic single crystals ($\kappa > 1$). Table 2 summarizes the different cases considered. Between the two possible mechanisms of twin partial plasticity (Eq. (11)), source-driven mechanism governs as $\tau_0^{\text{tp}} \ll g_z$ (Table 1).

Table 2 Void models in the present work

Case	λ_0 (nm)	$\kappa = \tau^{\beta}/\tau^{\alpha}$
Isotropic NT Crystals isoNT25, isoNT50, isoNT100	25, 50, 100	1.0, 1.0, 1.0
Anisotropic NT Crystals NT25, NT50, NT100	25, 50, 100	6.3, 4.5, 3.0
Isotropic Single Crystal	No twins	1.0
Anisotropic Single Crystals	No twins	6.3, 4.5, 3.0

4.1 Basic role of TB migration in porosity evolution

Before diving deeper into the mechanics of anisotropic porous NT microstructures, we set the stage by briefly discussing the size-dependent responses of isotropic twinned crystals with voids, hereafter referred to as isoNT materials.

The stress-strain responses (Fig. 2a) show a size-dependent yield followed by mild hardening that culminates into void-induced softening and ultimately, onset of failure (marked by X). The

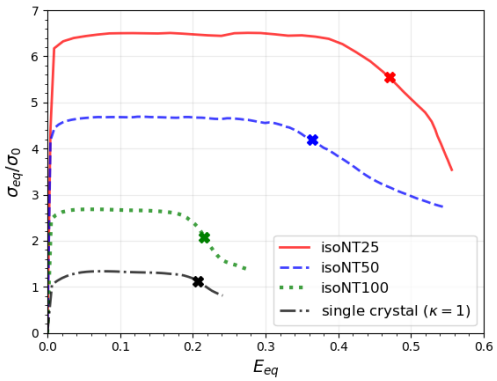

(a) Normalized stress-strain response

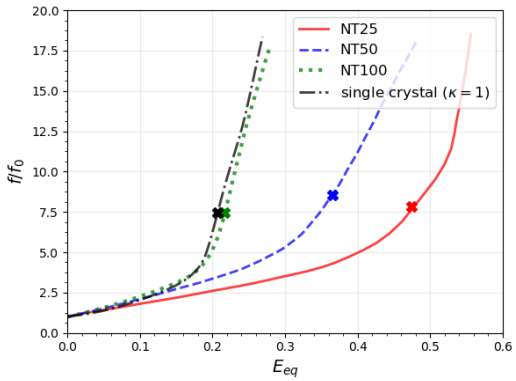

(b) Normalized porosity evolution

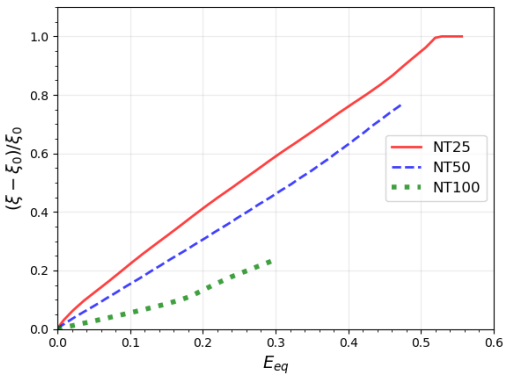

(c) Normalized twin volume fraction evolution

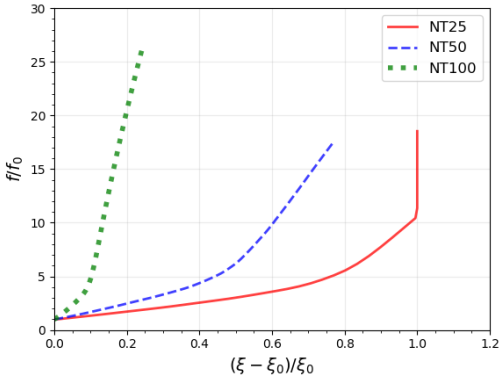

(d) Normalized porosity versus twin volume fraction

Figure 2 (a) Normalized stress-strain response and (b) porosity evolution characteristics of porous isoNT materials at $\mathcal{B} = 0$. Panel (c) shows the normalized twin volume fraction evolution (detwinning), and (d) shows the correlation between porosity evolution and detwinning.

corresponding *failure strain* (E^{c}_{eq}) is determined by the condition that the rate of lateral straining becomes zero [33], which signifies the onset of coalescence via intervoid ligament necking. The porosity evolution trends in Fig. 2b clearly show a delayed void growth with decreasing initial twin size.

Fig. 2c shows the twin size effect on detwinning in terms of the relative twin volume fraction, which occurs via TB migration. The detwinning rate increases with decreasing λ_0. In fact, the isoNT25 microstructure completely detwins at $E_{eq} = 0.52$. By extension, void growth and TB migration are coupled, which is reflected in Fig. 2d. It reveals that for smaller twin sizes (e.g., isoNT25), porosity evolution is dramatically slowed down as profuse detwinning occurs. On the other hand, porosity evolution is profuse when the detwinning rate is slow, e.g. isoNT100. Since the local twinning shear strain accrued by TB migration is $\gamma_{tw} = 1/\sqrt{2}$, the macroscopic shear strain due to TB migration is $(\xi - \xi_0)/\sqrt{2}$.

These trends remain valid at other $\mathcal{B}$ ratios and are discussed further in the context of the role of plastic anisotropy (Section 4.3).

4.2 Anisotropic porous NT microstructures

The grain-scale plastic anisotropy in actual NT materials often arises as the average twin size is generally smaller than the average grain size. Fig. 3 collates the stress-strain responses and the corresponding porosity evolution of porous NT microstructures under different biaxial stress ratios. For comparison, the isotropic porous single crystal responses are also shown; the stresses are normalized to the yield stress of the porous single crystal.

As in the isoNT case, these NT microstructures exhibit a Hall-Petch type strengthening at all levels of $\mathcal{B}$, Fig. 3a, 3c, 3e, and 3g. However, the post-yield responses and porosity evolution characteristics (Fig. 3b, 3d, 3f, and 3h) vary depending on λ_0 and $\mathcal{B}$.

At $\mathcal{B} = 0$, the NT100 stress-strain response resembles its isoNT counterpart with slightly extended regime before reaching failure strain, which correlates well with a delayed porosity evolution (Fig. 3b). The porosity evolution characteristics are consistent with the single crystal trends. On the other hand, NT50 and NT25 exhibit stress softening immediately following the yield with NT25 showing a more colossal softening than NT50. As discussed later, the stress softening results from an instability that arises due to the size-dependent crystallographic plastic anisotropy. Interestingly, NT50 and N25 also exhibit extended regimes of sluggish porosity evolution compared to NT100. Further, while the porosity evolution in NT50 is somewhat faster over much of the deformation regime, it is NT25 that meets the failure criterion earlier (denoted by X). This is because NT25 shows a rapid increase in porosity at $E_{eq} \sim 0.475$. As discussed later (cf. Fig. 4), the rapid porosity increase is a consequence of complete detwinning of the NT25 microstructure at that strain. With complete detwinning, the microstructure becomes a single crystal and the porosity growth rate mimics that of the single crystal. In comparison, detwinning rate is somewhat slower in NT50 to the extent that it serves beneficially in slowing down the porosity evolution (similar to isoNT50). The detwinning rate of NT100 is so slow that it does not have as strong an effect on porosity evolution as in NT50.

At higher biaxiality ratios (Fig. 3e-3h), the stress-strain and porosity evolution characteristics exhibit some important differences compared to $\mathcal{B} = 0$. With increasing $\mathcal{B}$ the porosity growth rate of NT50 and NT100 microstructures tend to approach or even exceed that of the isotropic single crystal. Further, in these cases stress softening correlates with faster porosity evolution with increasing $\mathcal{B}$ unlike the NT25 where stress softening occurs while the porosity evolution remains sluggish even at $\mathcal{B} = 0.2$. Only at $\mathcal{B} = 0.5$ does NT25 show a correlation between the stress softening and porosity evolution.

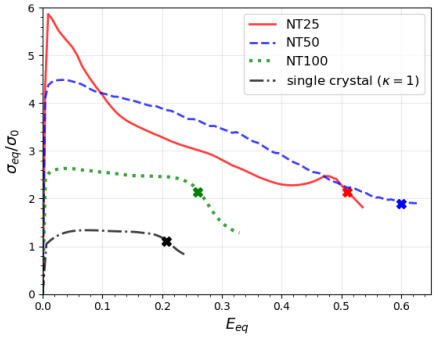

(a) $\mathcal{B} = 0.0$

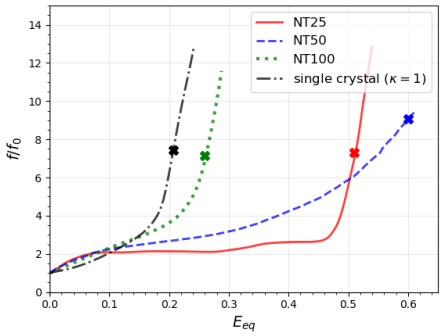

(b) $\mathcal{B} = 0.0$

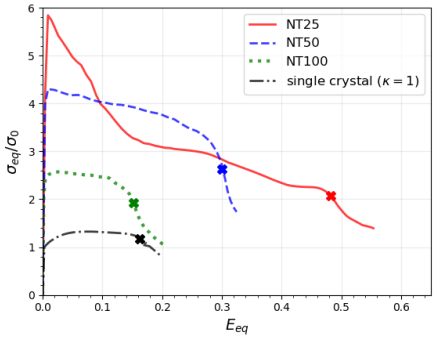

(c) $\mathcal{B} = 0.075$

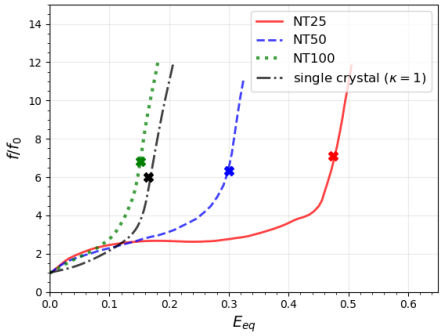

(d) $\mathcal{B} = 0.075$

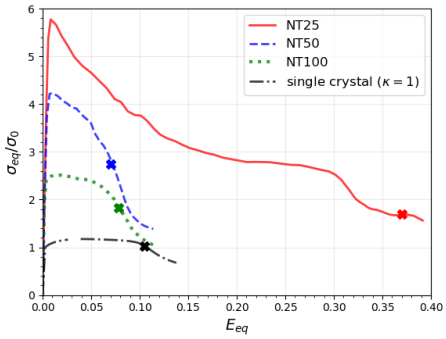

(e) $\mathcal{B} = 0.20$

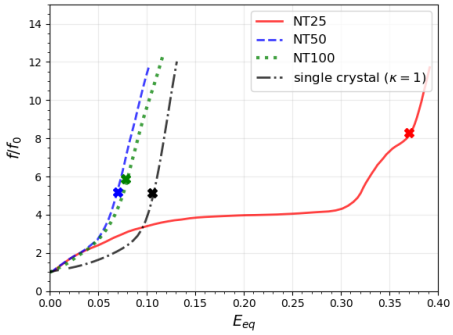

(f) $\mathcal{B} = 0.20$

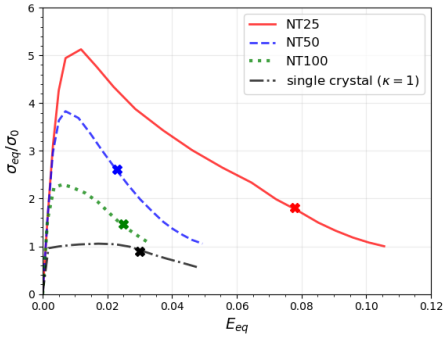

(g) $\mathcal{B} = 0.50$

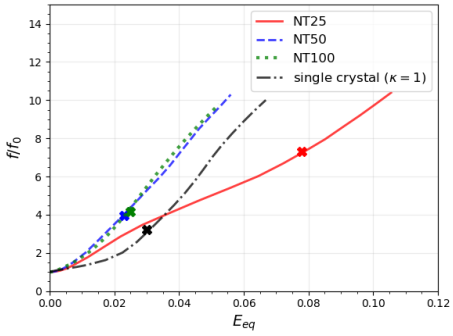

(h) $\mathcal{B} = 0.50$

Figure 3 Normalized stress-strain responses and porosity evolution at (a, b) $\mathcal{B} = 0$, (c, d) $\mathcal{B} = 0.075$, (e, f) $\mathcal{B} = 0.2$, and (g, h) $\mathcal{B} = 0.5$ for different NT microstructures. The initial porosity $f_0 = 0.7\%$. X indicates the onset of coalescence.

In the following paragraphs, we discuss the micromechanical underpinnings of these macroscopic trends.

Void growth is a result of plastic deformation in the surrounding matrix [57]. A salient characteristic of NT microstructures is the size-dependent TB migration [28], which serves as an additional mechanism of plastic deformation that modulates the role of the bulk plasticity in void growth. For illustration purposes, Fig. 4 shows the evolution of twins (blue regions) in the NT25 microstructure at $\mathcal{B} = 0.2$. TB migration causes gradual detwinning during which void evolution is negligible (cf. Fig. 4a and 4b). With complete detwinning the void grows rapidly, Fig. 4c. This reflects in the sluggishness followed by a runaway growth of the porosity curve in Fig. 3f. Although not shown here, similar characteristics are observed at $\mathcal{B} < 0.2$ in NT25, NT50, and to a lesser extent, in NT100. At $\mathcal{B} = 0.5$ the NT25 microstructure does not undergo complete detwinning prior to failure.

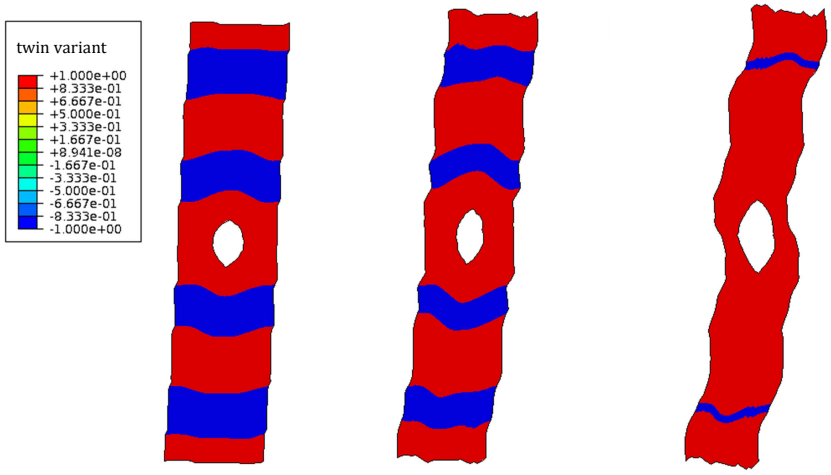

(a) $E_{22} = 0.05$ **(b)** $E_{22} = 0.15$ **(c)** $E_{22} = 0.3$

Figure 4 Twin boundary migration and void evolution in NT25 at $\mathcal{B} = 0.2$.

Fig. 5 compares the equivalent strain distributions in the NT100 and NT25 cases against the isotropic single crystal at $E_{22} = 0.15$ for $\mathcal{B} = 0.2$. In the single crystal and NT100 cases, significant void growth has occurred. This appears to be consistent with Nemat-Nasser and Hori [45] who investigated the role of crystallographic anisotropy in voided single crystals under plane strain condition. Plastic deformation is localized in the ligament separating the neighboring voids, which signifies internal necking [30, 33]. For the single crystal, a slip band emerges along the $[011](11\bar{1})$ slip system inclined at $\sim 70^\circ$ to the horizontal axis, Fig. 5a; in NT100, two nearly vertical deformation bands emanate from the void Fig. 5b, although they are quite weak.

In comparison, NT25 (and NT50, not shown here) shows a well-developed deformation band and a conjugate band that is less well developed, Fig. 5c. The deformation band accrues significant plastic strain in addition to the twinning plasticity. Note that at this strain level, there is no signature of strain localization in the inter-void ligament unlike NT100 and single crystal cases. A deeper crystallographic analysis, Fig. 6, reveals that the primary deformation band is a kink shear band [56], which deforms by coplanar slip (Fig. 6a). The contribution from the harder non-coplanar slip is negligible; Fig. 6b shows the shear strain on the most active non-coplanar (i.e., $[011](11\bar{1})$) slip system.

Given that no kink banding occurs in isoNT materials, we conclude that they result from

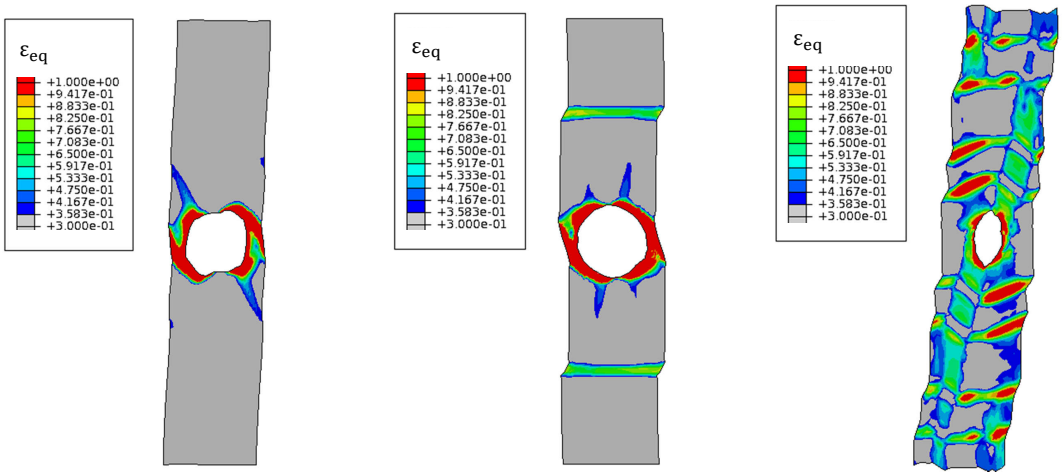

(a) isotropic single crystal **(b)** NT100 **(c)** NT25

Figure 5 Equivalent strain distribution (E_{eq}) at $E_{22} = 0.15$ in (a) isotropic single crystal, (b) NT100 and (c) NT25 at $\mathcal{B} = 0.2$.

the crystallographic plastic anisotropy (κ). These kink bands cause geometric softening, which manifests as rapid decrease in the macroscopic stress.

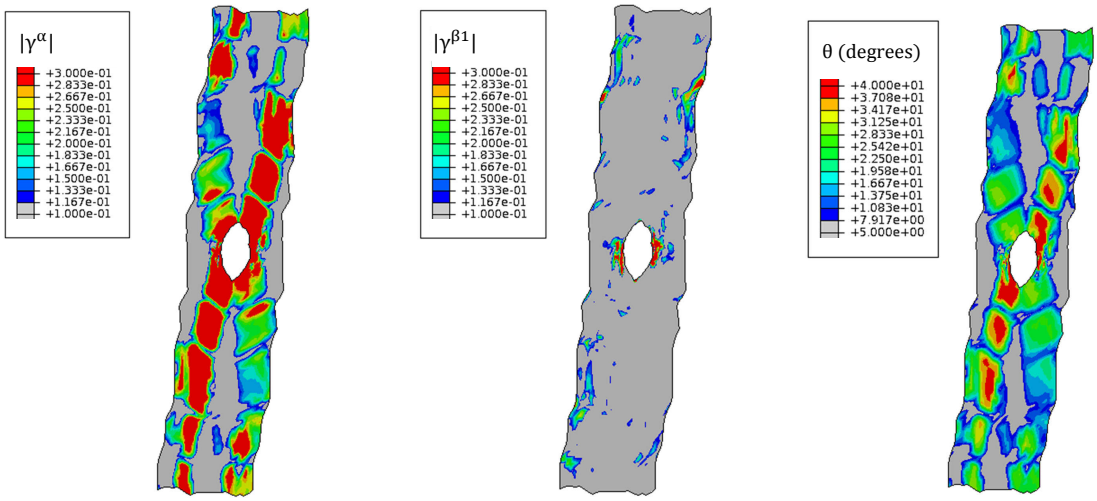

(a) coplanar slip **(b)** non-coplanar slip **(c)** lattice rotation

Figure 6 Micromechanical underpinnings of plastic deformation in NT25 at $\mathcal{B} = 0.2$. Panel (a) shows the accumulated shear strain on the $[0\bar{1}1](111)$ (coplanar) slip system. Panel (b) shows the accumulated shear strain on the most active $[011](11\bar{1})$ (non-coplanar) slip system. Panel (c) shows the lattice rotation.

Fig. 6c shows more intense lattice rotation in the kink band than the conjugate band. The magnitude of the lattice rotation inside the kink bands appears to be much higher compared to experiments on single crystals, e.g., Biswas et al. [5], Kysar and Briant [34], Patil et al. [49]. Although length-scale dependent simulations of a single crystal under uniaxial tension (no void) by Ling et al. [38] predict similar levels of lattice rotation, this aspect merits further investigation. One possibility is the role of latent hardening, which is not considered in the present work. Interacting

effects of latent hardening and plastic anisotropy may moderate the amount of lattice rotation and the resulting stress softening.

Collating these observations with the responses shown in Fig. 2 and Fig. 3, TB migration and plastic anisotropy (κ) play a role in porous NT responses in the following way. Recall that each TB migration event results in macroscopic plastic shear strain (cf. Section 2.2). Unlike bulk plasticity that provides the driving force for void growth, TB plasticity is dissociated from the void and remains restricted to the TB vicinity. At a given $\mathcal{B}$, it has a small, if any, contribution to void growth. Thus, with TB migration as a dominant plasticity mechanism the driving force for void growth effectively decreases, which causes delayed void growth as seen, for example, in the isoNT25 case. In addition to the TB migration effect, plastic anisotropy causes kink banding, which tends to stagnate the porosity evolution (e.g., NT25 in Fig. 3b) with concurrent stress softening (Fig. 3a). The propensity to kink band formation increases with κ but decreases with $\mathcal{B}$. This explains the persistent stress softening and sluggish void growth in NT25 over a wider range of $\mathcal{B}$ compared to NT50 and NT100, cf. Fig. 3. Moreover, in NT50 and NT100 the contribution to plasticity from TB migration is progressively smaller and hence, bulk plasticity contributes more to their porosity growth (at a given $\mathcal{B}$). Furthermore, with increasing $\mathcal{B}$ the lateral stress aids bulk plasticity thereby tempering the role of TB migration. Thus, the stress softening in NT50 and NT100 at $\mathcal{B} > 0.075$ is driven by faster porosity growth rather than kink band instability. In comparison, the stress softening NT25 is due to kink band for $\mathcal{B} \leq 0.2$ but primarily due to porosity growth for $\mathcal{B} = 0.5$.

Experimental studies have reported occurrence of kink bands in anisotropic single crystals near notches and voids [5, 11, 34, 49], in polycrystalline austenitic steels [14], and in metallic nanolaminates [46]. Length-scale dependent crystal plasticity models also predict their emergence in single crystals [38, 43], although they have not been reported in NT materials yet. Recent analytical calculations [47] indicate that in anisotropic perfectly plastic solids, near uniaxial plane strain tensile loading ($\mathcal{B} \approx 0$) parallel to the plane of plastic anisotropy can produce a shear band while those normal to the plane of anisotropy can produce a kink band. Indeed, our previous simulations on NT microstructures without voids [28] show no kink bands when loaded in tension parallel to the plane of anisotropy. Against that backdrop, the present results suggest that the presence of a defect such as void may cause a kink band even under tensile loading parallel to the plane of plastic anisotropy.

4.3 Anisotropy effect on NT ductility

With $\kappa = \sqrt{d/\lambda_0}$ being a measure of the grain-scale plastic anisotropy of an NT material, our preceding discussion reveals that for a given $\mathcal{B}$, there is threshold κ above which NT materials exhibit a slower porosity evolution relative to the isotropic single crystal. This motivates the following question: *to what extent is κ important in the porosity evolution in NT materials?*

Fig. 7 collates the porosity evolution characteristics of NT and isoNT materials at different levels of $\mathcal{B}$. At $\mathcal{B} = 0$ (Fig. 7a), the porosity evolution is slower in all NT microstructures (dashed curves) as compared to their isotropic counterparts (solid curves). At a mildly higher biaxiality ratio ($\mathcal{B} = 0.075$, Fig. 7b), the porosity growth in NT100 becomes faster relative to isoNT100, whereas NT50 and NT25 cases exhibit slower void growth compared isoNT50 and isoNT25 respectively. With increasing $\mathcal{B}$ (Fig. 7c, 7d), the NT microstructures show faster porosity evolution (relative to their isoNT counterparts) at progressively smaller λ_0 values; at $\mathcal{B} = 0.5$ all NT cases exhibit a faster porosity growth than their corresponding isoNT.

Fig. 8 consolidates the role of plastic anisotropy on the failure strain (E^c_{eq}) and the corresponding critical porosity (f_c) at the different biaxiality levels. In Fig. 8a, isoNT25 and NT25 microstructures show much larger failure strains compared to the single crystal persists over the range of $\mathcal{B}$ ratios

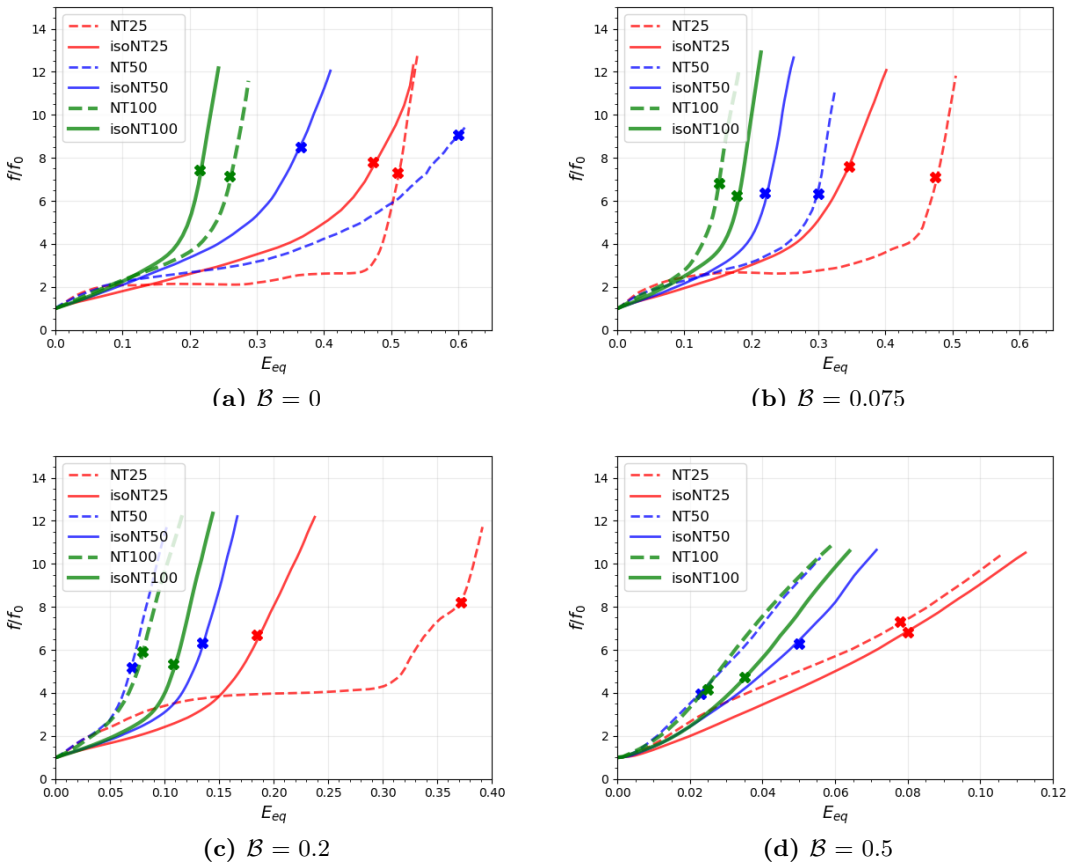

Figure 7 Normalized porosity evolution curves at (a) $\mathcal{B} = 0$, (b) $\mathcal{B} = 0.075$, (c) $\mathcal{B} = 0.2$, and, (d) $\mathcal{B} = 0.5$. Solid lines are for anisotropic NT materials and dashed lines are for isoNT cases.

with NT25 showing better resistance compared isoNT25. For NT50 and NT100, while plastic anisotropy delays failure at low $\mathcal{B}$ levels compared to their isoNT counterparts, the situation reverses with increasing $\mathcal{B}$. At $\mathcal{B} \gtrsim 0.2$, the NT50 and NT100 do not exhibit a major effect of twins on the failure strain relative to that of the single crystal. Thus, at a given $\mathcal{B}$ there appears to be a critical twin size (λ_0^c) that offers the largest failure strain; this λ_0^c decreases with increasing $\mathcal{B}$. Likewise, for a given λ_0 there is a critical biaxiality ratio ($\mathcal{B}_c$), above which plastic anisotropy may not be beneficial to ductility, although it may still offer a better performance than the single crystal.

In NT microstructures, $\mathcal{B}$ affects void growth in two ways. The lateral stress provides a net higher driving force for void growth relative to a uniaxial scenario, which promotes faster porosity evolution despite twin boundary migration. Further, as mentioned before it impedes the formation of kink bands, which also assists in the growth of void. This combined effect is much stronger at high levels of lateral stresses as evidenced for $\mathcal{B} = 0.5$.

As no kink bands form in isoNT materials, the size-dependent material hardening and TB migration resist the biaxiality effect on void growth. This creates an interesting interplay between twin boundary migration and $\mathcal{B}$ that governs their porosity evolution such that certain combinations of λ_0 and $\mathcal{B}$ offer better resistance to void growth than their anisotropic counterparts.

Fig. 8b shows the critical porosity, f_c, as a function of $\mathcal{B}$. Broadly speaking, the trends reveal that f_c is sensitive to λ_0 (both, isotropic and anisotropic cases) and $\mathcal{B}$. While the sensitivity to

$\mathcal{B}$ is much stronger for $\lambda_0 = 50$ nm and $\lambda_0 = 100$ nm (and these follow closely the trend for the isotropic single crystal), the small variations in the case of $\lambda_0 = 25$ nm may be important in the final fracture process [30].

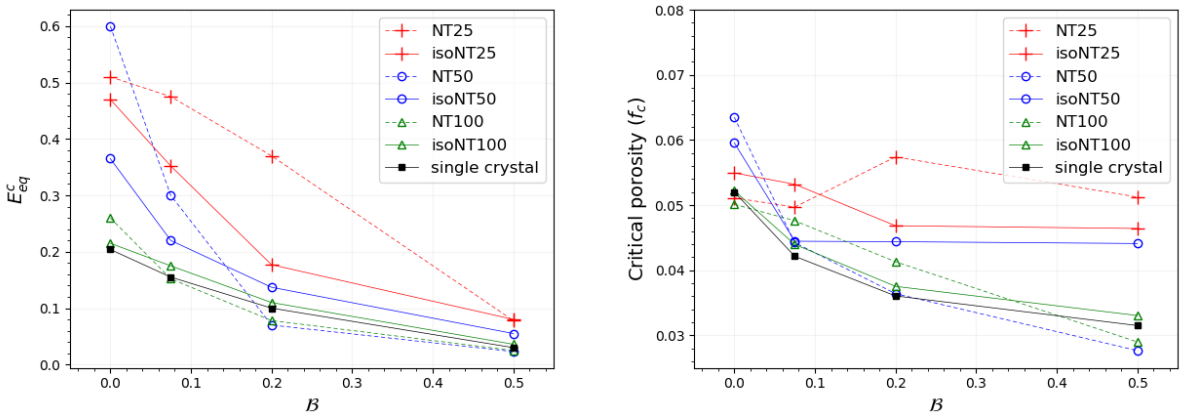

Figure 8 Dependence of (a) failure strain (E^c_{eq}) and (b) critical porosity (f_c) on twin size and biaxiality ratio for NT and isoNT microstructures. Isotropic single crystal results are also included as benchmark.

4.4 Role of twin boundary mobility

With the coupling of plastic anisotropy in the competing effects of the biaxiality ratio and TB migration on the porosity, it becomes imperative to ask: *how does twin boundary mobility affect the porosity evolution trends?* Twin boundary mobility is expressed as $V_{\text{tb}} = \dot{\gamma}_{\text{tp}}\lambda_0/\gamma_{\text{tw}}$ where $\dot{\gamma}_{\text{tp}}$ is given by Eq. (11). To understand this interaction, we performed additional calculations by modifying $\dot{\gamma}_0$ in Eq. (11)). In what follows, $V_{\text{tb}} = 1X$ corresponds to $\dot{\gamma}_0 = 1 \times 10^{-3}$ s^{-1} in Eq. (11), cf. Table 1, which serves as the reference case; by extension, $V_{\text{tb}} = 2X \iff \dot{\gamma}_0 = 2 \times 10^{-3}$ s^{-1}. We consider NT25 ($\kappa = 6.3$) and isoNT25 ($\kappa = 1$) as model cases and inspect their characteristics at two levels of $\mathcal{B}$.

First, we assess the coupling between the twin boundary mobility and plastic anisotropy at fixed $\mathcal{B} = 0.075$, Fig. 9a. For $V_{\text{tb}} = 1X$ (solid curves), increasing κ results in delayed porosity evolution. For $\kappa = 1$ (solid blue curve), the porosity evolution follows more or less conventional exponential growth. In comparison, kink band formation causes sluggish porosity growth for $\kappa = 6.3$ (solid red curve) over an extended deformation regime but transitions to a rapid growth at complete detwinning. For $V_{\text{tb}} = 2X$ (dashed curves), the porosity evolution profiles for $\kappa = 1$ (dashed blue curve) and 6.3 (dashed red curve) are nearly identical.

Fig. 9b shows the $\mathcal{B} - V_{\text{tb}}$ interaction effect on the porosity evolution at $\kappa = 6.3$ (i.e., NT25). While TB mobility effect is not significant at $\mathcal{B} = 0.075$, at $\mathcal{B} = 0.5$ the porosity evolution slows down appreciably with higher TB mobility. While increasing $\mathcal{B}$ provides a larger driving force for void growth, increasing TB mobility partially compensates this effect via increased TB plasticity.

These trends can be summarized as follows. We find that TB mobility plays a small role in the porosity evolution if kink bands occur, which is the case for NT materials with high κ or those subjected to low $\mathcal{B}$ levels. On the other hand, TB mobility plays a significant role in improving the ductility if kink bands do not occur, which is the case for NT materials with low $\kappa(\sim 1)$ values or those subjected to high $\mathcal{B}$ levels.

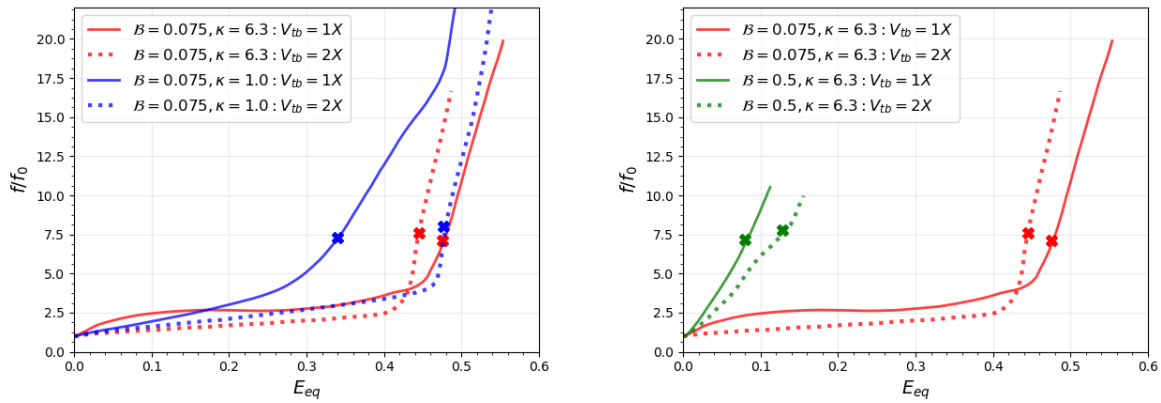

Figure 9 Effect of twin boundary mobility (V_{tb}) on porosity evolution in NT25 and isoNT25 for (a) fixed stress biaxiality ($\mathcal{B} = 0.075$) and (b) fixed plastic anisotropy ($\kappa = 6.3$).

We speculate that increasing TB mobility may be beneficial to ductility at larger λ_0. The rationale is that TB plasticity plays a smaller role in coarse-twinned microstructures (e.g., NT100) because detwinning is not as prominent as in fine-twinned (e.g., NT25) microstructures. Increasing the TB mobility of coarse-twinned microstructures will enhance the role of TB plasticity relative to the bulk plasticity, which will serve the purpose of shielding the void. This will be further aided by the fact that coarse-twinned microstructures (low κ) are less susceptible to kink bands than their fine-twinned counterparts.

4.5 Do twin boundaries matter?

The role of twin boundaries in the behavior can be assessed by comparing an NT response against an anisotropic single crystal for the same level of crystallographic anisotropy (κ). We set the ratio of the initial CRSS values of the non-coplanar to coplanar slip systems to 6.3. Fig. 10 illustrates this for NT25 at $\mathcal{B} = 0.2$ (with $V_{\text{tb}} = 1X$). The coplanar slip within the kink band is less intense in NT25 (Fig. 10a) than in the anisotropic single crystal with $\kappa = 6.3$ (Fig. 10b). Although not shown, the lattice rotation in the band is also much milder for NT25. By way of consequence, the stress softening in the NT material is milder (Fig. 10c) while the porosity evolution is somewhat more profuse (Fig. 10d) compared to its anisotropic single crystal counterpart.

With an initial twin volume fraction ξ_0, complete detwinning of the crystal translates to a macroscopic strain $E_{\text{tw}} \sim \xi_0 \gamma_{\text{tw}}$ solely via TB migration. Thus, if complete detwinning occurs before void coalescence the corresponding macroscopic strain at coalescence (E^{c}_{eq}) will be (at least) equal to E_{tw}. This is most clearly seen in Fig. 2 for isoNT25 and, to some extent, isoNT50 where $E^{c}_{\text{eq}} \gtrsim E_{\text{tw}}$. Coupled with TB mobility effects, the spatial (e.g., gradient versus random) and size distributions of twins are expected to play a role in the porosity evolution, and therefore, the macroscale tensile ductility [28, 73].

The focus of this work has been on the micromechanics of void growth. The predicted failure strains and critical porosities (Fig. 8) are tied to the coalescence onset criterion based on internal ligament necking. These trends may be affected if alternate coalescence modes were to occur. For instance, kink bands in the case of $\kappa = 6.3$ at $\mathcal{B} \lesssim 0.2$ may cause premature failure by shear bands [3]. Investigating the role of material microstructure in such failure mechanisms is beyond the scope

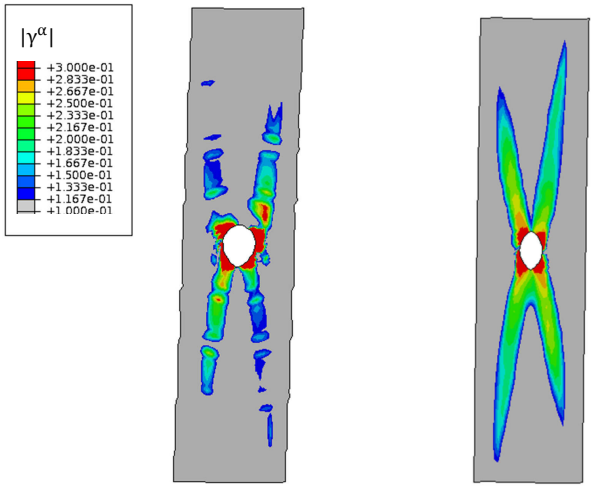

(a) NT25 **(b)** anisotropic single crystal, $\kappa = 6.3$

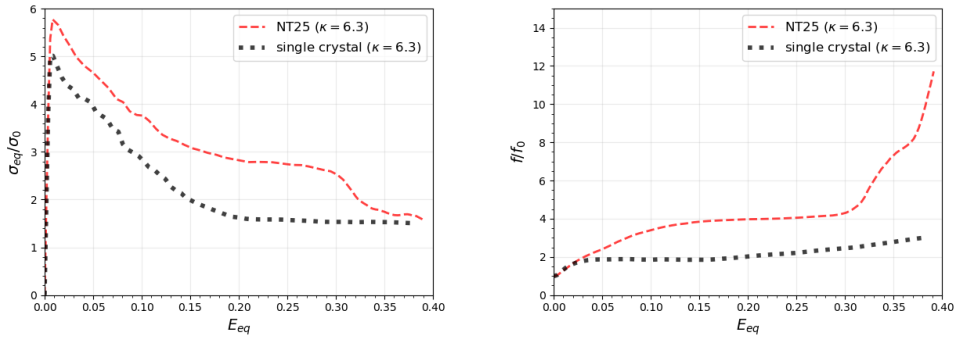

(c) **(d)**

Figure 10 Role of twin boundaries ($\mathcal{B} = 0.2$). The kink band is less intense with milder coplanar slip in NT25 (Panel a) compared to the anisotropic single crystal with same level of κ (Panel b). Results are shown at $E_{22} = 0.05$. Panels (c) and (d) highlight the effect of twin boundaries in the stress-strain and porosity evolution, respectively.

of this work.

The critical porosity values (Fig. 8b) translate to critical void sizes of $\sim 20 - 25$ nm over the ranges of λ_0 and $\mathcal{B}$, which are on the same order as or smaller than the initial twin thicknesses (25-100 nm). In experiments (e.g., Qin et al. [55]) the dimple sizes on the fractured surfaces are orders of magnitude bigger than the twin thickness. This discrepancy suggests that fracture processes in real NT materials could evolve differently as voids grow. One possibility, for example, is that as voids grow, they may impinge on to the twin boundaries, and damage may then evolve either via necking of twin lamellas or via crack propagation along twin boundaries [32]. Such processes can result in surface roughness that exceeds the twin and grain sizes.

5 Concluding remarks

In this work, we present a length-scale dependent crystal plasticity analysis of void growth in a nanotwinned material under controlled biaxial tensile stress states. We investigate the role of twin size (and the resulting crystallographic plastic anisotropy) as well as the effect of twin boundary migration on void evolution characteristics. We also present a detailed micromechanical analysis that governs the macroscopic behaviors are elucidated. Twin boundaries are crucial beyond merely characterizing the grain-scale plastic anisotropy as they qualitatively affect void growth via TB migration. The main observations are:

1. isoNT microstructures exhibit delayed porosity evolution with decreasing initial twin size. By extension, the strain to failure increases with decreasing twin size. This is a result of detwinning due to TB migration, which becomes more potent with decreasing twin size.

2. Anisotropic NT microstructures broadly exhibit porosity trends similar to isoNT counterparts, although crystallographic plastic anisotropy causes kink bands, which complicate the role of TB migration on the size-dependent failure. The propensity of kink bands correlates with crystallographic plastic anisotropy. Together with TB migration, kink bands cause a sluggish porosity evolution while simultaneously causing stress softening. In isoNT microstructures, kink bands do not occur and the delayed porosity evolution is a result of size-dependent TB migration.

3. For a fixed biaxiality ratio, there is a critical twin size below which failure is delayed relative to the isotropic single crystal. This critical twin size decreases with increasing biaxiality ratio.

4. The type (i.e., a combination of twin size and plastic anisotropy) of NT microstructures that offers the best resistance to damage by void growth depends on the stress state. Broadly speaking, plastically anisotropic microstructures with fine twins may be desirable.

5. TB mobility affects the role of crystallographic plastic anisotropy and biaxiality ratio in failure. Optimal TB mobility is a design factor that should be chosen based on the initial twin size as it will modulate the rate of detwinning, which in turn will influence void growth.

Moving forward, modeling fully three-dimensional scenarios with different crystallographic orientations (which may lead to inclined twin boundaries) and more general stress states would provide deeper insights. Such investigations will pave the way to formulating microstructually-informed reduced-order representations of damage plasticity, although they are computationally non-trivial. More sophisticated and efficient computational approaches such as phase-field modeling may be

needed to accommodate such complications. Even in the two-dimensional setting, modeling inclined TBs and TB migration toward the void are computationally thornier. Further, novel deformation mechanisms and modes of damage may emerge, whose role in damage tolerance needs to be explored.

Acknowledgement

SPJ acknowledges the financial support provided by the National Science Foundation under Grant Number CMMI-1932976. KJ acknowledges support from NUS Research Scholarship.

Appendix A Calculation of slip gradients

The calculation of slip gradients at every gauss point is implemented within an Abaqus user defined material subroutine (UMAT). In this approach, we exploit the concept of shape functions for evaluating the slip gradients corresponding to each slip system. As an illustrative example, we present the methodology for a 4-node plane strain finite element, but the approach can be adapted to other types of elements. In a UMAT, the values of state dependent variables, such as slip, are calculated at each Gauss integration point. Within an element, we create a 4-noded pseudo-element described by linear shape functions (Fig. A.1) by joining the integration points. To enable this calculation, we store the values of slip at the nodes of the pseudo-element (viz. integration points of element) in an array declared in the CommonVars module; this allows access to the values of slip at all nodes of a pseudo-element even when the UMAT subroutine is called for one particular integration point.

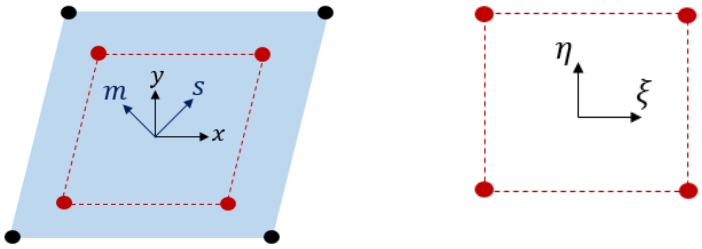

Figure A.1 (a) A pseudo-element defined by joining the integration points (in red) of a standard element. (b) The pseudo-element is used to calculate gradients in isoparameteric coordinates which are then transformed to cartesian coordinates.

The gradient of slip in cartesian coordinates within the pseudo-element is calculated using the derivatives of shape functions ($\boldsymbol{N}^p$) of the pseudo-element,

$$\frac{\partial \gamma^\alpha}{\partial x} = \sum_{i=1}^{4} \frac{\partial N_i^p}{\partial x} \gamma_i^\alpha \tag{14}$$

$$\frac{\partial \gamma^\alpha}{\partial y} = \sum_{i=1}^{4} \frac{\partial N_i^p}{\partial y} \gamma_i^\alpha \tag{15}$$

where N_i^p and γ_i^α are the shape function and slip on the i^{th} pseudo-node, respectively. These spatial derivatives of the shape functions in Cartesian coordinates are in turn calculated from the derivatives in the local isoparamteric coordinates using the determinant of the Jacobian matrix ($\boldsymbol{J}$),

$$\begin{bmatrix} \frac{\partial}{\partial x} \\ \frac{\partial}{\partial y} \end{bmatrix} = \boldsymbol{J}^{-1} \begin{bmatrix} \frac{\partial}{\partial \xi} \\ \frac{\partial}{\partial \eta} \end{bmatrix} \tag{16}$$

Finally, the slip gradient in the slip direction $\boldsymbol{s^\alpha}$ is calculated using the chain rule,

$$\boldsymbol{\nabla}\gamma^\alpha = \frac{\partial \gamma^\alpha}{\partial x}\frac{\partial x}{\partial \boldsymbol{s^\alpha}} + \frac{\partial \gamma^\alpha}{\partial y}\frac{\partial y}{\partial \boldsymbol{s^\alpha}} \tag{17}$$

References

[1] Anderoglu, O., Misra, A., Wang, H., Zhang, X., 2008. Thermal stability of sputtered cu films with nanoscale growth twins. Journal of Applied Physics 103, 094322.

[2] Asaro, R.J., Suresh, S., 2005. Mechanistic models for the activation volume and rate sensitivity in metals with nanocrystalline grains and nano-scale twins. Acta Materialia 53, 3369–3382.

[3] Benzerga, A., Thomas, N., Herrington, J.S., 2019. Plastic flow anisotropy drives shear fracture. Scientific reports 9, 1–9.

[4] Beyerlein, I., Demkowicz, M., Misra, A., Uberuaga, B., 2015. Defect-interface interactions. Progress in Materials Science 74, 125–210.

[5] Biswas, P., Narasimhan, R., Kumar, A., 2013. Interaction between a notch and cylindrical voids in aluminum single crystals: experimental observations and numerical simulations. Journal of the Mechanics and Physics of Solids 61, 1027–1046.

[6] Biswas, P., Narasimhan, R., Tewari, A., 2011. Influence of crack tip constraint on void growth in ductile fcc single crystals. Materials Science and Engineering: A 528, 823–831.

[7] Borg, U., Niordson, C.F., Kysar, J.W., 2008. Size effects on void growth in single crystals with distributed voids. International Journal of Plasticity 24, 688–701.

[8] Bufford, D., Wang, H., Zhang, X., 2013. Thermal stability of twins and strengthening mechanisms in differently oriented epitaxial nanotwinned ag films. Journal of Materials Research 28, 1729–1739.

[9] Cheng, Y., Jin, Z.H., Zhang, Y., Gao, H., 2010. On intrinsic brittleness and ductility of intergranular fracture along symmetrical tilt grain boundaries in copper. Acta Materialia 58, 2293–2299.

[10] Cheng, Z., Zhou, H., Lu, Q., Gao, H., Lu, L., 2018. Extra strengthening and work hardening in gradient nanotwinned metals. Science 362.

[11] Crone, W., Shield, T., 2001. Experimental study of the deformation near a notch tip in copper and copper–beryllium single crystals. Journal of the Mechanics and Physics of Solids 49, 2819–2838.

[12] Cuitino, A., Ortiz, M., 1996. Ductile fracture by vacancy condensation in fcc single crystals. Acta Materialia 44, 427–436.

[13] Dao, M., Lu, L., Shen, Y., Suresh, S., 2006. Strength, strain-rate sensitivity and ductility of copper with nanoscale twins. Acta materialia 54, 5421–5432.

[14] Di Gioacchino, F., da Fonseca, J.Q., 2015. An experimental study of the polycrystalline plasticity of austenitic stainless steel. International Journal of Plasticity 74, 92–109.

[15] Evans, A.G., Hutchinson, J.W., 2009. A critical assessment of theories of strain gradient plasticity. Acta Materialia 57, 1675–1688.

[16] Fleck, N., Hutchinson, J., 1997. Strain gradient plasticity. Advances in Applied Mechanics 33, 296–361.

[17] Fleck, N., Hutchinson, J., 2001. A reformulation of strain gradient plasticity. Journal of the Mechanics and Physics of Solids 49, 2245–2271.

[18] Gallican, V., Hure, J., 2017. Anisotropic coalescence criterion for nanoporous materials. Journal of the Mechanics and Physics of Solids 108, 30–48.

[19] Gludovatz, B., Hohenwarter, A., Catoor, D., Chang, E.H., George, E.P., Ritchie, R.O., 2014. A fracture-resistant high-entropy alloy for cryogenic applications. Science 345, 1153–1158.

[20] Gurtin, M.E., Anand, L., Lele, S.P., 2007. Gradient single-crystal plasticity with free energy dependent on dislocation densities. Journal of the Mechanics and Physics of Solids 55, 1853–1878.

[21] Han, C.S., Gao, H., Huang, Y., Nix, W.D., 2005. Mechanism-based strain gradient crystal plasticity. I. Theory. Journal of the Mechanics and Physics of Solids 53, 1188–1203.

[22] Huang, Y., 1991. A user-material subroutine incroporating single crystal plasticity in the ABAQUS finite element program. Harvard Univ. Cambridge.

[23] Huang, Y., Gao, H., Nix, W., Hutchinson, J., 2000. Mechanism-based strain gradient plasticity—II. Analysis. Journal of the Mechanics and Physics of Solids 48, 99–128.

[24] Hussein, M., Borg, U., Niordson, C.F., Deshpande, V., 2008. Plasticity size effects in voided crystals. Journal of the Mechanics and Physics of Solids 56, 114–131.

[25] Jang, D., Li, X., Gao, H., Greer, J.R., 2012. Deformation mechanisms in nanotwinned metal nanopillars. Nature Nanotechnology 7, 594–601.

[26] Jerusalem, A., Dao, M., Suresh, S., Radovitzky, R., 2008. Three-dimensional model of strength and ductility of polycrystalline copper containing nanoscale twins. Acta Materialia 56, 4647–4657.

[27] Joshi, K., 2018. On Deformation Stability and Ductile Damage in Nanotwinned Metals. Ph.D. thesis. National University of Singapore.

[28] Joshi, K., Joshi, S.P., 2017. Interacting effects of strengthening and twin boundary migration in nanotwinned materials. Journal of the Mechanics and Physics of Solids 101, 180–196.

[29] Ke, X., Ye, J., Pan, Z., Geng, J., Besser, M.F., Qu, D., Caro, A., Marian, J., Ott, R.T., Wang, Y.M., et al., 2019. Ideal maximum strengths and defect-induced softening in nanocrystalline-nanotwinned metals. Nature Materials 18, 1207–1214.

[30] Keralavarma, S., Hoelscher, S., Benzerga, A., 2011. Void growth and coalescence in anisotropic plastic solids. International Journal of Solids and Structures 48, 1696–1710.

[31] Khavasad, P.H., Keralavarma, S.M., 2021. Effective yield criterion for a porous single crystal accounting for void size effects. Mechanics of Materials 160.

[32] Kim, S.W., Li, X., Gao, H., Kumar, S., 2012. In situ observations of crack arrest and bridging by nanoscale twins in copper thin films. Acta Materialia 60, 2959–2972.

[33] Koplik, J., Needleman, A., 1988. Void growth and coalescence in porous plastic solids. International Journal of Solids and Structures 24, 835–853.

[34] Kysar, J.W., Briant, C.L., 2002. Crack tip deformation fields in ductile single crystals. Acta Materialia 50, 2367–2380.

[35] Li, X., Dao, M., Eberl, C., Hodge, A.M., Gao, H., 2016. Fracture, fatigue, and creep of nanotwinned metals. MRS Bulletin 41, 298–304.

[36] Li, X., Wei, Y., Lu, L., Lu, K., Gao, H., 2010. Dislocation nucleation governed softening and maximum strength in nano-twinned metals. Nature 464, 877–880.

[37] Ling, C., Besson, J., Forest, S., Tanguy, B., Latourte, F., Bosso, E., 2016. An elastoviscoplastic model for porous single crystals at finite strains and its assessment based on unit cell simulations. International Journal of Plasticity 84, 58–87.

[38] Ling, C., Forest, S., Besson, J., Tanguy, B., Latourte, F., 2018. A reduced micromorphic single crystal plasticity model at finite deformations. application to strain localization and void growth in ductile metals. International Journal of Solids and Structures 134, 43–69.

[39] Lu, K., 2016. Stabilizing nanostructures in metals using grain and twin boundary architectures. Nature Reviews Materials 1, 1–13.

[40] Lu, K., Lu, L., Suresh, S., 2009. Strengthening materials by engineering coherent internal boundaries at the nanoscale. Science 324, 349–352.

[41] Lu, L., Shen, Y., Chen, X., Qian, L., Lu, K., 2004. Ultrahigh strength and high electrical conductivity in copper. Science 304, 422–426.

[42] Ma, E., Zhu, T., 2017. Towards strength–ductility synergy through the design of heterogeneous nanostructures in metals. Materials Today 20, 323–331.

[43] Marano, A., Gélébart, L., Forest, S., 2021. Fft-based simulations of slip and kink bands formation in 3d polycrystals: influence of strain gradient crystal plasticity. Journal of the Mechanics and Physics of Solids 149, 104295.

[44] Mirkhani, H., Joshi, S.P., 2014. Mechanism-based crystal plasticity modeling of twin boundary migration in nanotwinned face-centered-cubic metals. Journal of the Mechanics and Physics of Solids 68, 107–133.

[45] Nemat-Nasser, S., Hori, M., 1987. Void collapse and void growth in crystalline solids. Journal of Applied Physics 62, 2746–2757.

[46] Nizolek, T., Begley, M., McCabe, R., Avallone, J., Mara, N., Beyerlein, I., Pollock, T., 2017. Strain fields induced by kink band propagation in cu-nb nanolaminate composites. Acta Materialia 133, 303–315.

[47] Nizolek, T.J., Pollock, T.M., McMeeking, R.M., 2021. Kink band and shear band localization in anisotropic perfectly plastic solids. Journal of the Mechanics and Physics of Solids 146, 104183.

[48] Ovid'Ko, I., Sheinerman, A., Skiba, N., 2011. Elongated nanoscale voids at deformed special grain boundary structures in nanocrystalline materials. Acta Materialia 59, 678–685.

[49] Patil, S.D., Narasimhan, R., Mishra, R.K., 2009. Observation of kink shear bands in an aluminium single crystal fracture specimen. Scripta Materialia 61, 465–468.

[50] Peirce, D., Asaro, R.J., Needleman, A., 1982. An analysis of nonuniform and localized deformation in ductile single crystals. Acta Metallurgica 30, 1087–1119.

[51] Pineau, A., Benzerga, A.A., Pardoen, T., 2016a. Failure of metals i: Brittle and ductile fracture. Acta Materialia 107, 424–483.

[52] Pineau, A., Benzerga, A.A., Pardoen, T., 2016b. Failure of metals iii: Fracture and fatigue of nanostructured metallic materials. Acta Materialia 107, 508–544.

[53] Potirniche, G., Hearndon, J., Horstemeyer, M., Ling, X., 2006. Lattice orientation effects on void growth and coalescence in fcc single crystals. International Journal of Plasticity 22, 921–942.

[54] Qi, W., Bertram, A., 1999. Anisotropic continuum damage modeling for single crystals at high temperatures. International Journal of Plasticity 15, 1197–1215.

[55] Qin, E., Lu, L., Tao, N., Tan, J., Lu, K., 2009. Enhanced fracture toughness and strength in bulk nanocrystalline Cu with nanoscale twin bundles. Acta Materialia 57, 6215–6225.

[56] Rice, J.R., 1987. Tensile crack tip fields in elastic-ideally plastic crystals. Mechanics of Materials 6, 317–335.

[57] Rice, J.R., Tracey, D.M., 1969. On the ductile enlargement of voids in triaxial stress fields. Journal of the Mechanics and Physics of Solids 17, 201–217.

[58] Sansoz, F., Lu, K., Zhu, T., Misra, A., 2016. Strengthening and plasticity in nanotwinned metals. MRS Bulletin 41, 292–297.

[59] Scherer, J.M., Besson, J., Forest, S., Hure, J., Tanguy, B., 2021. A strain gradient plasticity model of porous single crystal ductile fracture. Journal of the Mechanics and Physics of Solids 156, 104606.

[60] Singh, A., Tang, L., Dao, M., Lu, L., Suresh, S., 2011. Fracture toughness and fatigue crack growth characteristics of nanotwinned copper. Acta Materialia 59, 2437–2446.

[61] Sinha, T., Kulkarni, Y., 2014. Alternating brittle and ductile response of coherent twin boundaries in nanotwinned metals. Journal of Applied Physics 116, 183505.

[62] Song, D., Castañeda, P.P., 2017a. A finite-strain homogenization model for viscoplastic porous single crystals: I–theory. Journal of the Mechanics and Physics of Solids 107, 560–579.

[63] Song, D., Castañeda, P.P., 2017b. A finite-strain homogenization model for viscoplastic porous single crystals: Ii–applications. Journal of the Mechanics and Physics of Solids 107, 580–602.

[64] Song, D., Castañeda, P.P., 2018a. A multi-scale homogenization model for fine-grained porous viscoplastic polycrystals: I–Finite-strain theory. Journal of the Mechanics and Physics of Solids 115, 102–122.

[65] Song, D., Castañeda, P.P., 2018b. A multi-scale homogenization model for fine-grained porous viscoplastic polycrystals: II–Applications to FCC and HCP materials. Journal of the Mechanics and Physics of Solids 115, 77–101.

[66] Srivastava, A., Needleman, A., 2015. Effect of crystal orientation on porosity evolution in a creeping single crystal. Mechanics of Materials 90, 10–29.

[67] Tekoglu, C., Leblond, J.B., Pardoen, T., 2012. A criterion for the onset of void coalescence under combined tension and shear. Journal of the Mechanics and Physics of Solids 60, 1363–1381.

[68] Uberuaga, B., Hoagland, R., Voter, A., Valone, S., 2007. Direct transformation of vacancy voids to stacking fault tetrahedra. Physical Review Letters 99, 135501.

[69] Wang, J., Misra, A., 2011. An overview of interface-dominated deformation mechanisms in metallic multilayers. Current Opinion in Solid State and Materials Science 15, 20–28.

[70] Wang, Y.M., Sansoz, F., LaGrange, T., Ott, R.T., Marian, J., Barbee, T.W., Hamza, A.V., 2013. Defective twin boundaries in nanotwinned metals. Nature materials 12, 697–702.

[71] Wei, Q., Cheng, S., Ramesh, K., Ma, E., 2004. Effect of nanocrystalline and ultrafine grain sizes on the strain rate sensitivity and activation volume: fcc versus bcc metals. Materials Science and Engineering: A 381, 71–79.

[72] Wei, Y., 2011. Scaling of maximum strength with grain size in nanotwinned fcc metals. Physical Review B 83, 132104.

[73] Wei, Y., Li, Y., Zhu, L., Liu, Y., Lei, X., Wang, G., Wu, Y., Mi, Z., Liu, J., Wang, H., et al., 2014. Evading the strength–ductility trade-off dilemma in steel through gradient hierarchical nanotwins. Nature Communications 5, 1–8.

[74] Wu, X.L., Liao, X.Z., Srinivasan, S.G., Zhou, F., Lavernia, E.J., Valiev, R.Z., Zhu, Y.T., 2008. New deformation twinning mechanism generates zero macroscopic strain in nanocrystalline metals. Physical Review Letters 100, 95701.

[75] Xiao, Y., Nielsen, K., Niordson, C., 2021. Size effect on void coalescence under intense shear. European Journal of Mechanics-A/Solids , 104329.

[76] Xiong, L., You, Z., Qu, S., Lu, L., 2018. Fracture behavior of heterogeneous nanostructured 316l austenitic stainless steel with nanotwin bundles. Acta Materialia 150, 130–138.

[77] Yerra, S., Tekoglu, C., Scheyvaerts, F., Delannay, L., Van Houtte, P., Pardoen, T., et al., 2010. Void growth and coalescence in single crystals. International Journal of Solids and Structures 47, 1016–1029.

[78] You, Z., Li, X., Gui, L., Lu, Q., Zhu, T., Gao, H., Lu, L., 2013. Plastic anisotropy and associated deformation mechanisms in nanotwinned metals. Acta Materialia 61, 217–227.

[79] You, Z., Qu, S., Luo, S., Lu, L., 2019. Fracture toughness evaluation of nanostructured metals via a contactless crack opening displacement gauge. Materialia 7, 100430.

[80] Yuan, F., Wu, X., 2013. Atomistic scale fracture behaviours in hierarchically nanotwinned metals. Philosophical Magazine 93, 3248–3259.

[81] Zeng, Z., Li, X., Lu, L., Zhu, T., 2015. Fracture in a thin film of nanotwinned copper. Acta Materialia 98, 313–317.

[82] Zhang, Z., Sheng, H., Wang, Z., Gludovatz, B., Zhang, Z., George, E.P., Yu, Q., Mao, S.X., Ritchie, R.O., 2017. Dislocation mechanisms and 3D twin architectures generate exceptional strength-ductility-toughness combination in CrCoNi medium-entropy alloy. Nature Communications 8, 1–8.

[83] Zheng, H., Wang, J., Huang, J.Y., Wang, J., Mao, S.X., 2014. Void-assisted plasticity in Ag nanowires with a single twin structure. Nanoscale 6, 9574–9578.

[84] Zhou, H., Qu, S., Yang, W., 2010. Toughening by nano-scaled twin boundaries in nanocrystals. Modelling and Simulation in Materials Science and Engineering 18, 065002.

[85] Zhu, L., Qu, S., Guo, X., Lu, J., 2015. Analysis of the twin spacing and grain size effects on mechanical properties in hierarchically nanotwinned face-centered cubic metals based on a mechanism-based plasticity model. Journal of the Mechanics and Physics of Solids 76, 162–179.

[86] Zhu, L., Ruan, H., Li, X., Dao, M., Gao, H., Lu, J., 2011a. Modeling grain size dependent optimal twin spacing for achieving ultimate high strength and related high ductility in nanotwinned metals. Acta Materialia 59, 5544–5557.

[87] Zhu, T., Gao, H., 2012. Plastic deformation mechanism in nanotwinned metals: An insight from molecular dynamics and mechanistic modeling. Scripta Materialia 66, 843–848.

[88] Zhu, T., Li, J., Samanta, A., Kim, H.G., Suresh, S., 2007. Interfacial plasticity governs strain rate sensitivity and ductility in nanostructured metals. Proceedings of the National Academy of Sciences of the United States of America 104, 3031–3036.

[89] Zhu, Y.T., Wu, X., Liao, X., Narayan, J., Kecskes, L., Mathaudhu, S., 2011b. Dislocation–twin interactions in nanocrystalline fcc metals. Acta Materialia 59, 812–821.